Engineering the interfaces in MgO-modified Ni/Al_2O_3 for CO_2 methanation

Yufei Xie, Servaas Lips, Lennert D'ooghe, Maarten Sabbe, Christophe Detavernier, Hilde Poelman, Vladimir Galvita

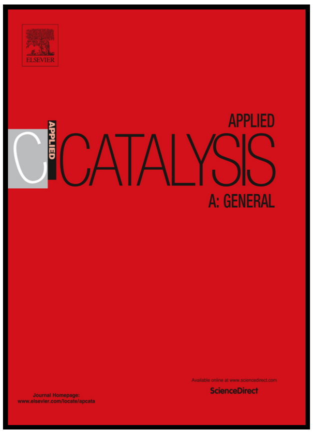

PII: S0926-860X(24)00361-2

DOI: https://doi.org/10.1016/j.apcata.2024.119916

Reference: APCATA119916

To appear in: *Applied Catalysis A, General*

Received date: 24 June 2024
Revised date: 20 August 2024
Accepted date: 23 August 2024

Please cite this article as: Yufei Xie, Servaas Lips, Lennert D'ooghe, Maarten Sabbe, Christophe Detavernier, Hilde Poelman and Vladimir Galvita, Engineering the interfaces in MgO-modified Ni/Al_2O_3 for CO_2 methanation, *Applied Catalysis A, General,* (2024) doi:https://doi.org/10.1016/j.apcata.2024.119916

Engineering the interfaces in MgO-modified Ni/Al_2O_3 for CO_2 methanation

Yufei Xie [a], *Servaas Lips* [a], *Lennert D'ooghe* [a], *Maarten Sabbe* [a], *Christophe Detavernier* [b], *Hilde Poelman* [a], *Vladimir Galvita* [a,]*

[a] Laboratory for Chemical Technology, Ghent University, Tech Lane Ghent Science Park A 125, B-9052 Ghent, Belgium

[b] Department of Solid State Sciences, Ghent University, Krijgslaan 281, S1, B-9000 Ghent, Belgium

* Corresponding author: Vladimir Galvita, Vladimir.Galvita@UGent.be

ABSTRACT: The interaction between metallic active phases and oxides is of great significance for catalytic properties, but still remains elusive. Here, two reverse interfaces are constructed (Ni/MgO and MgO/Ni on Al_2O_3) for a typical CO_2 methanation catalyst, Ni/Al_2O_3, by depositing Ni and MgO in opposite sequences on Al_2O_3. Enhanced performance was found on both interface structures, however, distinct turnover frequencies indicate different mechanisms. With MgO present in between Ni and Al_2O_3, the formation of an inactive $NiAl_2O_4$ spinel phase is mitigated, making more NiO available for reduction. When MgO is added on top of Ni, the new MgO/Ni interface exhibits high reactivity in CO_2 methanation. CO_2 temperature programmed desorption, in situ quick X-ray adsorption spectroscopy (QXAS) and modulation excitation XAS (MEXAS) demonstrate that a Ni-NiO redox mechanism occurs with enhanced CO_2 activation at the MgO/Ni interface. The subsequent hydrogenation of adsorbed carbon monoxide and carbonate species requires nearby Ni to provide H spillover and occurs preferably at the interface sites, where adsorbed species are more easily activated. Hence, interfaces between the same compounds, but with reverse structures, result in different phenomena, illustrating the role an interface structure can play in catalytic systems.

KEY WORDS: CO_2 methanation, interface, magnesium oxide, nickel, aluminum oxide

1. INTRODUCTION

Supported metal catalysts—including dispersed metal species on high-surface-area materials such as oxides, carbons, and zeolites—are widely used in catalytic applications. These high-surface-area materials, termed as supports or carriers, provide a platform for the fine dispersion of metals, resulting in stable metal nanoparticles. This configuration allows for the formation of catalytically active sites that are resistant to sintering during reaction. Subsequent investigations demonstrate the existence of metal–support interactions, which significantly and distinctly influence the geometric structures and electronic properties of the supported metals, consequently affecting their catalytic performance. The metal-oxide interface is particularly important as it often provides additional sites where chemical reactions can take place[1, 2]. This interface is where the active metal and oxide meet and interact, giving rise to new physical and chemical properties that differ from the surface characteristics of the individual materials [1, 3]. The structure of the interface varies: the oxide part can be a support, giving mechanical strength and/or ensuring fine dispersion of the active metal phase, but also a modifying phase, aimed at providing sites with tuned activity[4]. Ideally, the catalyst configuration can be classified as traditional supported catalyst (metal supported on oxide) and inverse catalyst (oxide supported on metal)[2]. However, in many cases, identifying the support phase or modifier can be a dilemma. Sometimes, it is obvious as in the case where metal particles are present on a planar solid slab or wafer (Figure 1(a)). At times, the term ‘support’ can also be somewhat ambiguous when the phase consists of equally sized or smaller particles than the active phase, surrounding or decorating the latter (Figure 1(b)). One could argue that typically the support is present in larger amounts than the active phase, though this is not always the case[5]. Hence, the boundary between support and modifying oxide can be a thin line.

The interaction between active metal nanoparticles and oxides, as support and/or oxide modifier, can induce a variety of effects at the interface, including charge transfer[6-8], reshaping of the nanoparticles by the support[9, 10], creation of new (mixed) phases[11-13], and the formation of highly active (adsorption) sites at the interfacial perimeter[14]. In literature, Metal-Support Interactions (MSI) are recognized, with two concepts being particularly notable. The first is Strong Metal-Support Interaction (SMSI), wherein the support is actually covering part of the active metal, a concept initially introduced to explain the diminished chemisorption capacity of noble metals on TiO_2 following reduction treatments[15, 16]. The second is Electronic Metal-Support Interaction (EMSI), highlighting the role of chemical bonding and charge transfer at the metal-support interface in modifying the electronic and chemical properties on the surface of metal particles[7, 17]. As indicated above, these interactions are in fact not limited to *metal on support* configurations, but can be extended to any metal-oxide interface, regardless of the function and position of the oxide.

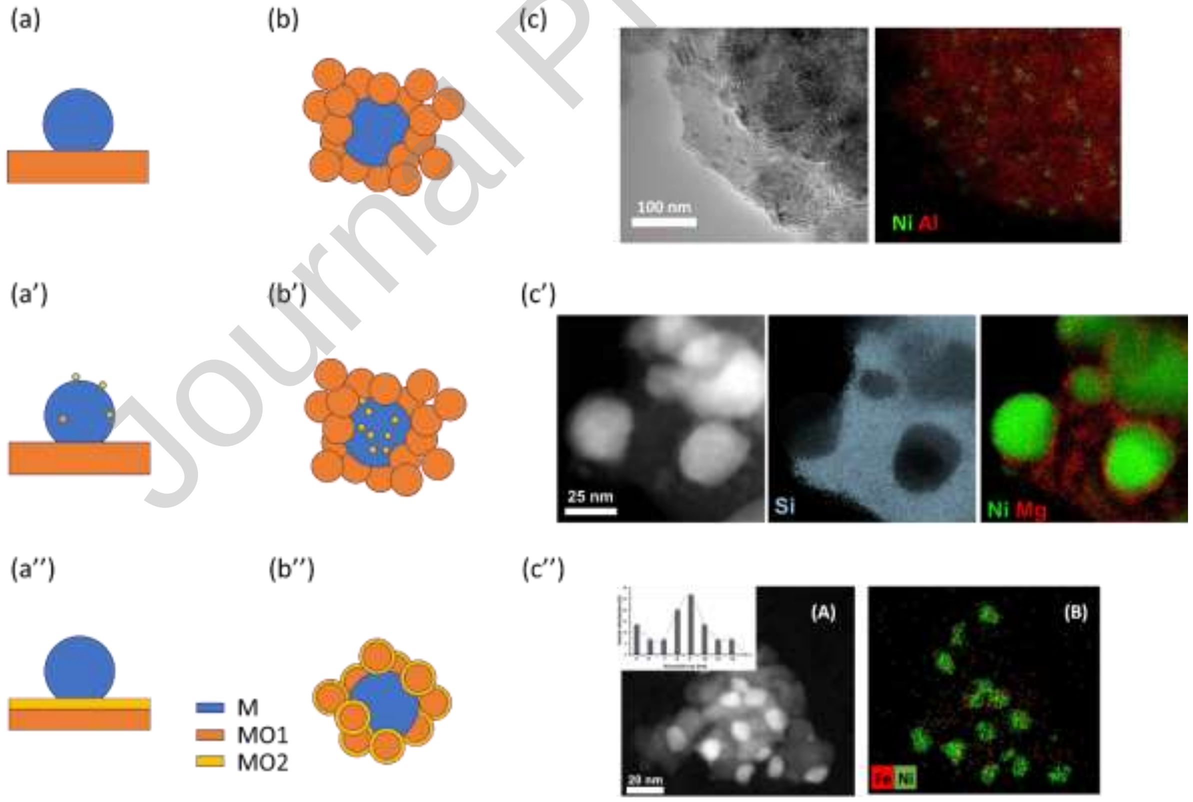

Figure 1. Metal-oxide interactions: (a): metal particle (M) supported on an oxide slab (MO1), B: metal particle surrounded by support particles (MO1); (a'), (b'): deposition of an extra modifying oxide (MO2) after the metal deposition; (a''), (b''): deposition of an extra modifying

oxide (MO2) before the metal deposition (MO1); (c): HRTEM of 9wt%Ni/$MgAl_2O_4$ with EDX overlay mapping of Ni and Al[18]; (c'): MgO/Ni/SiO_2 (1.5wt% Mg, 15wt% Ni) with extra MgO decorating the Ni particles[19]; (c"): reduced Ni/$MgFeAlO_4$ (8wt%Ni, 1wt%Fe) with extra Fe incorporated into the $MgAl_2O_4$ support to modify the Ni properties after reduction by Ni-Fe alloying[20]. M: metal, MO1: metal oxide 1, MO2: metal oxide 2.

The characteristics of the interface, such as its chemical composition, structural properties, and electronic state, can significantly influence the catalytic activity and selectivity. As a result, tailoring the metal-oxide interface is a crucial strategy in designing and developing novel catalysts with enhanced catalytic efficiency. For instance, Ni is always proposed as a good CO_2 methanation catalyst, but pure metallic Ni catalyzes the reverse water-gas shift reaction producing CO, rather than CH_4[21]. Along the same line, experimental works report that high CO selectivity is observed when Ni is supported on SiO_2, an oxide weakly interacting with Ni, so that mainly the performance of metallic Ni itself is playing[19, 22]. In contrast, when Ni interacts with oxides like MgO[19, 23], Al_2O_3[9, 24, 25] or CeO_2[26], strong interaction is observed, which modifies the properties of metallic Ni and leads to achieving high CH_4 selectivity. For enhancing CO_2 conversion using Ni-based catalysts, understanding the intricate catalyst structure, interactions at the interface and their relationship with the methanation activity is key.

Researchers have been exploring ways to control the surface/interface structures to finetune performance. To manage these metal-oxide interactions, various approaches have been adopted, such as adjusting the support's composition, morphology, or surface traits, and altering the metals' size and composition[27, 28], along with changing pretreatment methods like thermal procedures, redox cycles, and adsorbate-induced alterations[29-31]. In addition, one can purposely create new interfaces or modify existing ones, by adding an extra oxide to the catalytic system. The latter can either be applied on top of the metal surface (Figure 1(a'), (b'), (c')), or on the support to change the metal-support interaction (Figure 1(a"), (b"), (c")). For instance, Yan et al.[32] utilized different elements to create Ni-FeO_x and Ni-ZrO_2 interfaces, influencing CO and CH_4 formation differently due to the varying CO adsorption strengths on Ni-FeO_x and Ni-ZrO_2. Various combinations of Ni with other oxides, like Ni-MnO_x[11-13] and Ni-MgO[23], have been explored to develop new interfaces. In a recent study, MgO-modified Ni depositing on SiO_2, a support showing limited interaction with the active metal, was investigated as a model system. The enhanced CH_4 selectivity was attributed to the MgO/Ni interface (Figure 1(a') and (c'))[19].

While much research has investigated altering the interface nature, the effect of the spatial structure of these interfaces and the link between different spatial structures and performances remains a complex, yet vital, area of study. In this work, the effect of interface spatial arrangement is investigated with CO_2 methanation as a probe reaction. Ni/Al_2O_3, a widely applied and economically interesting, selective yet less active catalyst[33, 34], is decorated by MgO for constructing interfaces with synergies [19, 23]. The spatial structure of the MgO/Ni interface is engineered to fabricated two interfaces with reverse spatial structure and the consequent metal-oxide interactions are studied. By maintaining the same elemental composition, interfaces with contrasting structures, namely Ni/MgO and MgO/Ni on an Al_2O_3 support, are fabricated. The catalytic performance and turnover frequency (TOF) of these interfaces are then assessed and a suite of characterization methods is employed to analyze the interfaces of these inversely arranged MgO-Ni and Ni-MgO catalysts, uncovering their distinctive properties in the context of CO_2 activation. To probe the potential mechanisms at play, diffuse reflectance infrared Fourier transform spectroscopy (DRIFTS) is used, alongside modulation excitation X-ray absorption spectroscopy (MEXAS).

2. MATERIALS AND METHODS

2.1 Catalyst Synthesis

All samples were prepared by sequential incipient wetness impregnation. γ-Al_2O_3 (Samsol, Puralox Scca-150/200), $Ni(NO_3)_2.6H_2O$ (99.99%, Sigma-Aldrich) and $Mg(NO_3)_2.9H_2O$ (99%, Sigma-Aldrich) were used as support and precursors, respectively. The latter were dissolved in deionized water, preparing the required precursor solutions for further use.

Two different impregnation sequences were applied in this work. For the forward sequence, Ni is impregnated first on γ-Al_2O_3, followed by MgO. In a typical synthesis process, 4.37 g of $Ni(NO_3)_2{\cdot}6H_2O$ was dissolved in a certain amount of water, leading to a solution with a volume of 5 mL. The solution was added dropwise to 5.00 g of γ-Al_2O_3. Hereafter, the sample was dried at 120 °C overnight, ground and calcined at 600 °C for 2h. These catalysts are labeled as 15Ni/Al, where 15 stands for the weight percentage of Ni, i.e. 15 wt% (metal base). Then, specific amounts of $Mg(NO_3)_2{\cdot}6H_2O$ (0.53 g and 2.77 g for Mg loadings of 1 and 5 %, respectively) were dissolved in a certain amount of water, leading to the solution with a volume of 5 mL. The solution was added dropwise to 5.00 g 15Ni/Al. Again, the samples were dried at 120 °C overnight, ground and calcined at 600 °C for 2h. These catalysts are labeled as xMg15Ni/Al, where x stands for the weight percentage of Mg (metal base, x=1 and 5wt%). For the reverse sequence, MgO is impregnated first on γ-Al_2O_3, yielding xMgAl, followed by NiO with the same intermediate treatments. The latter catalysts are labeled as 15Ni/xMgAl (metal base, x=1 and 5).

A control group using $MgAl_2O_4$ as support for Ni was prepared via co-precipitation from an aqueous solution of $Mg(NO_3)_2.6H_2O$ (99%, Sigma-Aldrich) and $Al(NO_3)_3.9H_2O$ (98.5%, Sigma-Aldrich). The molar ratio between Mg/Al equals 1/2. NH_4OH (ACS reagent, 28.0-30.0% NH_3 basis) was added dropwise to the precursor solution to adjust the pH to 10. During precipitation, the temperature was kept at 60 °C. The precipitate was subsequently aged overnight at room temperature. Next, it was filtered, washed with deionized water and dried overnight at 120 °C. After drying, the precipitate powder was calcined in air at 800 °C for 5h. Ni was then impregnated on $MgAl_2O_4$, following the above-mentioned method.

2.2 Characterization

X-ray diffraction (XRD) analyses were performed on a Siemens Diffractometer Kristalloflex D5000 with Cu Kα radiation ($\lambda = 0.154$ nm). The information of crystallite size can be extracted from the XRD pattern via the Scherrer equation:

$$L = \frac{0.9\lambda}{\beta \cos \theta} \tag{1}$$

where L is the mean size of the crystallite in nm, β is the full width at half maximum (FWHM), λ is the wavelength of the X-rays and θ the Bragg angle. The FWHM used in the Scherrer equation is determined by fitting a Gaussian function to the second most intense diffraction peak Ni(200) as the most intense one Ni(111) overlaps with a diffraction peak of γ-Al_2O_3.

N_2 physisorption-desorption experiments were conducted in a Micromeritics Tristar 3000 analyzer. The surface area was calculated using the Brunauer−Emmett−Teller (BET) method.

Scanning Electron Microscopy equipped with Energy Dispersive X-ray spectrometry (SEM-EDX) was used to analyze the element composition of the samples. These measurements were conducted in a JEOL JSM 5400 setup equipped with an INCA x-act extension (Oxford instruments). Beam energies of 5 keV and 20 keV were applied to vary the information depth.

X-ray photoelectron spectroscopy (XPS) was conducted on a S-Probe XPS spectrometer (VG, Surface Science Instruments), equipped with a monochromatized Al Kα source (hν = 1486 Ev).

The binding energies were calibrated using the C 1s peak of adventitious carbon at 285 Ev as a reference.

Temperature-programmed H_2 reduction (H_2-TPR), CO_2-temperature programmed desorption (CO_2-TPD) and H_2 chemisorption experiments were carried out in a Micromeritics AutoChem II chemisorption analyzer. Typically, 100 mg of sample was used for one test.

For H_2-TPR, the sample was pretreated at 600 °C for 30 min and cooled down to 50 °C in Ar. Then, the sample was heated to 600 °C (or 900 °C) in 5 vol.% H_2/Ar (60 mL/min) and held at this temperature for 30 min. The reduction degree was calculated as in equation (2).

$$Reduction\ degree = \frac{measured\ H_2\ consumption}{theoretical\ H_2\ consumption} \times 100\% \qquad (2)$$

For H_2 chemisorption, the sample was pre-reduced in 5 vol.% H_2/Ar (60 mL/min) at 600 °C for 30 min. A pure Ar (60 mL/min) purge then followed with the aim of removing H_2 adsorbed during reduction. After cooling down to 50 °C, 5 vol.% H_2/Ar was pulsed over the catalyst until the peak area detected at the outlet became constant. Using a stoichiometric ratio equal to 1 between adsorbed H and Ni[35], the number of active Ni sites was determined.

For CO_2-TPD, the sample was pre-reduced in 5 vol.% H_2/Ar (60 mL/min) at 600 °C for 30 min. A pure He (60 mL/min) purge was then sent with the aim of removing H_2 adsorbed during reduction. CO_2 adsorption was carried out at 300 °C – the reaction temperature. Then, the sample was cooled down to 50 °C, still in the CO_2 atmosphere. After purging with He for 30 min, the sample was heated to 600 °C with a rate of 10 °C/min. The outlet of the reactor was connected to an online mass spectrometer (MS, Pfeiffer Vacuum OmniStar QMS 301). The desorbing gases were analyzed by tracking He, H_2O, CO and CO_2 signals at 4 AMU (atomic mass unit), 18 AMU, 28 AMU and 44 AMU, respectively.

Diffuse reflectance infrared Fourier transform spectroscopy (DRIFTS) was performed on a Bruker Tensor 27 spectrometer equipped with a mercury–cadmium–telluride (MCT) detector. Typically, the diluted sample (1:20 KBr) was pre-treated with a H_2-TPR process up to 500 °C in H_2/He (90 mL/min, H_2:He=1:5). After cool down to room temperature (RT), the background spectrum was collected. Next, the sample was exposed to a pure CO_2 flow, ramping the temperature to 500 °C and then purging with He for 1 h. After cool down to RT, DRIFT spectra were collected. Then, a temperature programmed surface reaction with H_2 (H_2-TPSR) was applied with a ramp of 10 °C /min up to 600 °C under H_2/He (90 mL/min, H_2:He=1:5), after which spectra were collected after cooling down to RT.

In situ Ni K edge quick X-ray absorption spectroscopy (QXAS) experiments were performed at the ROCK beamline of the French synchrotron SOLEIL (2.75 GeV, 450 Ma)[36]. All spectra were calibrated by simultaneously measuring a Ni foil. During the experiments, spectra were collected with an acquisition speed of 2 Hz. The sample was loaded in a 1.2 mm quartz capillary and implemented in a dedicated frame connected to gas feed lines through Swagelok fittings. XAS acquisition was performed under a 7 mL/min total flow rate. H_2-TPR was performed under 5 vol.% H_2/He up to 600 °C at a heating rate of 10 °C/min, where the temperature was held for 30 min. After cool down, CO_2-TPO experiments were run under pure CO_2 up to 600 °C and held for 30 min. A steady-state methanation process (CO_2:H_2:He=1:4:5) at 300 °C was implemented for 60 min on reduced samples after a H_2-TPR to 600 °C. After methanation, modulation excitation XAS (MEXAS) experiments were carried out at 300 °C, keeping the H_2 flow constant at 2.8 mL /min and varying the CO_2 flow between 2.8 and 0 mL /min, balanced with He, see Figure S1. A total of 15 periods were applied during the experiment. The data were analyzed by phase sensitive detection (PSD). The details of this analyzing method are described in the work of De Coster et al.[37].

2.3 Catalytic Performance Tests

Catalytic performance tests were run at 300 °C and 1 bar in a fixed-bed reactor (inner diameter = 7 mm, length = 47 cm). For each experiment, 100 mg catalyst (particle size 100-200 μm) mixed with 500 mg α-Al_2O_3 (as dilution) was loaded into the reactor. The temperature of the catalyst bed was monitored by a K-type thermocouple. The sample was first reduced under H_2/Ar mixture (H_2:Ar = 4:5, total flow = 180 mL/min) at 600 °C for 30 min (pre-reaction treatment). After reduction, the catalyst bed was cooled down to 300 °C. Subsequently, the gas was switched to CO_2:H_2:Ar (CO_2:H_2:Ar = 1:4:5, total flow = 200 mL/min) for the methanation reaction. An online gas chromatograph (GC, ThermoFisher Scientific, Trace 1310) was used to analyze the concentrations of different gases in the outlet stream. Products were separated by a Molsieve 5A and a Hayesep-N column and monitored with a thermal conductivity detector (TCD). The conversion of CO_2, selectivity to CH_4 and CO, and reaction rate are calculated as follows:

$$\mathrm{CO_2\ Conversion} = \frac{\mathrm{F_{CO2,in}} - \mathrm{F_{CO2,out}}}{\mathrm{F_{CO2,in}}} \times 100\% \tag{3}$$

$$\mathrm{CH_4\ Selectivity} = \frac{\mathrm{F_{CH4,out}}}{\mathrm{F_{CH4,out}} + \mathrm{F_{CO,out}}} \times 100\% \tag{4}$$

$$\mathrm{CO\ Selectivity} = \frac{\mathrm{F_{CO,out}}}{\mathrm{F_{CH4,out}} + \mathrm{F_{CO,out}}} \times 100\% \tag{5}$$

$$\mathrm{Reaction\ rate} = \frac{\mathrm{F_{CO2,in}} - \mathrm{F_{CO2,out}}}{\mathrm{m_{catalyst}} \times 22.4 \times 1000 \times 60} \tag{6}$$

and the carbon balance is calculated as follows:

$$\mathrm{Carbon\ balance} = \frac{F_{CO2,out} + F_{CH4,out} + F_{CO,out}}{F_{CO2,in}} \times 100\% \tag{7}$$

where $F_{i,in}$ (mL/min) and $F_{i,out}$ (mL/min) stand for the inlet and the outlet flow rate of gas i. $m_{catalyst}$ (g) stands the amount of catalyst loading in the reactor. The carbon balance for all the tests was higher than 99.5 %.

Turnover frequencies (TOF, 1/s) were determined on the basis of exposed Ni (mol/g), calculated from the result of the H_2-chemisorption experiments.

$$\mathrm{TOF} = \frac{\text{Reaction rate}}{\text{amount of Ni exposed}} \tag{8}$$

3. RESULTS AND DISCUSSION

3.1 Catalytic Performance of the Two Interface Types

15Ni/Al, prepared by directly impregnating $Ni(NO_3)_2.6H_2O$ onto Al_2O_3, was considered as a standard. Two approaches were applied to modify the interfaces present. First, the Ni/Al_2O_3 interface was modified by applying MgO onto Al_2O_3 before impregnating the Ni precursor, i.e.15Ni/xMgAl; Second, new MgO/Ni interfaces were created by introducing the MgO precursor onto 15Ni/Al, i.e. xMg15Ni/Al. For both sample types, x amounts to 1 or 5wt%.

The physicochemical properties of these samples are listed in Table 1. All the samples with Al_2O_3 support show a surface area higher than 100 m^2/g. Adding MgO reduces the surface area, which is more pronounced when the Mg loading increases to 5 %. The reference sample with $MgAl_2O_4$ support shows a lower surface area of 57 m^2/g. The Ni particle size is generally considered as a significant factor for methanation performance[28, 38-40]. In this work, however, the Ni particle sizes of the samples studied are similar, as suggested by the crystallite sizes from XRD (Figure S2) and the metal dispersion (Table 1), indicating that MgO hardly affects the Ni particle size, whatever its location.

Table 1. Physicochemical properties of the catalysts after calcination (surface area) and after reduction (reduction degrees, exposed Ni sites and Ni crystallite size). Reduction conditions: 5 vol.% H_2/Ar, 60 mL/min at 600 °C for 30 min.

Sample	Surface area (m^2/g)	Reduction degree (%)[a]	Dispersion (%)[b]	Exposed Ni ($x10^{-5}$ mol Ni/g)[b]	Crystallite size Ni (nm)[c]
15Ni/Al	140	28	7.0	1.0	6.6 ± 0.2
15Ni/1MgAl	140	48	6.0	2.0	-
15Ni/5MgAl	119	40	5.9	1.7	6.2 ± 0.1
1Mg15Ni/Al	157	23	6.5	0.9	-
5Mg15Ni/Al	117	15	6.0	0.7	6.3 ± 0.5
15Ni/$MgAl_2O_4$	57	31	3.8	2.8	5.9 ± 0.1

[a] determined by H_2-TPR under the same condition as the pre-reduction process before reaction.

[b] estimated by H_2-chemisorption.

[c] determined by XRD after reduction; samples with 1Mg were not tested.

The CO_2 methanation reactivity of the catalysts was measured at 300 °C and ambient pressure after reduction at 600 °C. All samples are very selective towards CH_4, showing a CH_4 selectivity above 90%. A considerable improvement in reaction rate was observed over the 15Ni/xMgAl samples (Figure 2(a)). The primary factor distinguishing the performance of 15Ni/Al and 15Ni/xMgAl (regardless of the MgO loading) is the difference in exposed metallic Ni, going up from 1 $x10^{-5}$ mol Ni/g to ~2 $x10^{-5}$ mol Ni/g upon addition of MgO (Table 1). The intrinsic activity or TOF of 15Ni/xMgAl is comparable to that of 15Ni/Al, but because of the doubled amount of exposed Ni sites, the reaction rate increases.

The CO_2 reaction rate continued to increase along with the amount of MgO. Since the amount of exposed Ni in 15Ni/5MgAl is almost similar to the one for 15Ni/1MgAl, there must be a different mechanism at play. The latter is evidenced in the intrinsic activity of 15Ni/5MgAl being higher than for 15Ni/1MgAl, likely due to more Ni contacting with MgO and/or a higher intrinsic activity of these interface sites, making the 15Ni/5MgAl activity rise above the one of 15Ni/1MgAl. In view of practical application, stability test results of the samples are displayed in Figure S3, with no apparent deactivation observed during the 12-hour test. This indicates the created MgO/Ni interface maintains its activity over longer time.

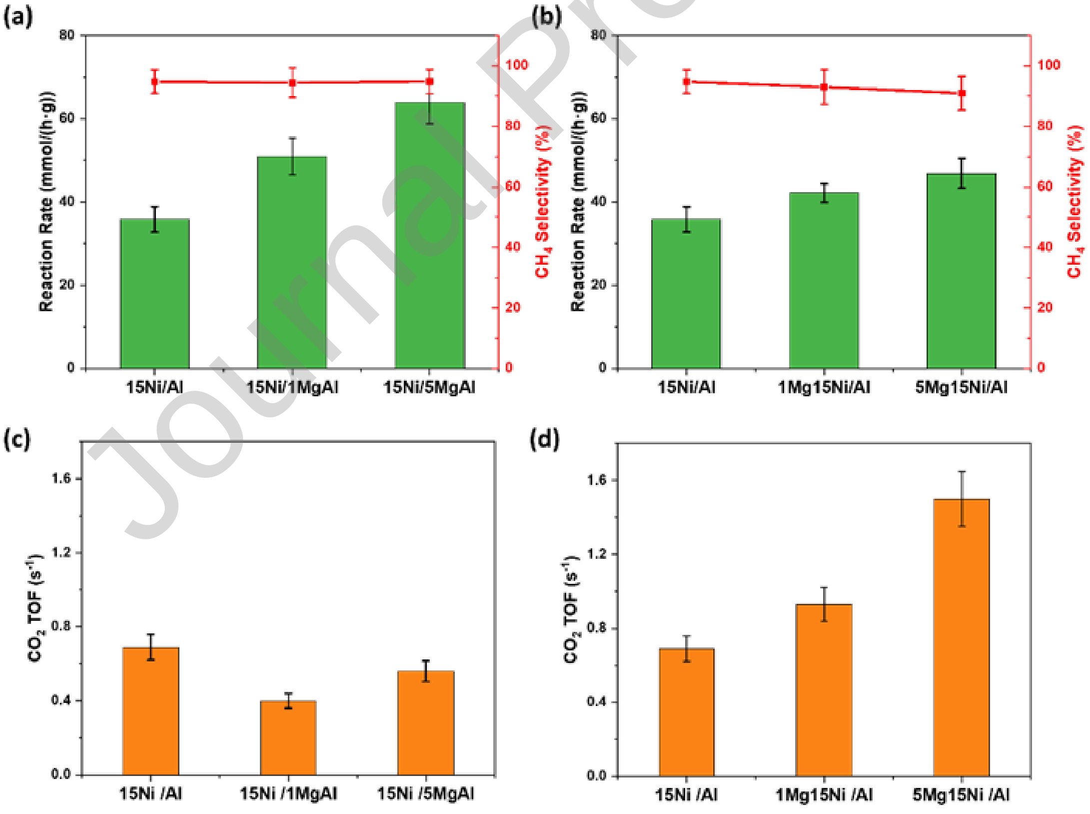

Figure 2. Catalytic performance test with (a-b) reaction rate per gram of catalyst and CH_4 selectivity and (c-d) TOF of pre-reduced 15Ni/Al, 15Ni/1MgAl, 15Ni/5MgAl (a,c) and 15Ni/Al,

1Mg15Ni/Al, 5Mg15Ni/Al (b,d). Reaction conditions: 0.1 g pre-reduced catalyst, 300 °C, CO_2:H_2:Ar = 1:4:5, flow rate CO_2 = 20 mL/min, ambient pressure.

3.2 Adding MgO onto the support – Ni/MgAl

The structure of the 15Ni/Al and 15Ni/xMgAl catalysts was characterized by XRD. NiO is detected on the as-prepared 15Ni/Al (15Ni/Al-ap) (Figure S4(a)) in addition to alumina diffractions. The Al_2O_3(440) diffraction peak for 15Ni/Al-ap displays a left shift compared with the pure γ-Al_2O_3 support (Figure S4(b)). This can point to the incorporation of larger Ni^{2+} (83 pm) cations into the lattice of γ-Al_2O_3 (Al^{3+}: 67.5 pm), resulting in a unit cell expansion. 15Ni/Al was then reduced using the same conditions as for the pre-reaction treatment, i.e. at 600 °C (15Ni/Al-red). For 15Ni/Al-red, the peaks of NiO (43.3° and 62.8°) disappear, while metallic Ni appears (at 44.5° and 51.8°). However, the shift of the Al_2O_3(440) diffraction peak remains unchanged, suggesting that incorporated Ni^{2+} remains stable.

The full XRD patterns of xMgAl and 15Ni/xMgAl are displayed in Figure S5, with Figure 3 zooming in on the Al_2O_3(440) and NiO(200) diffractions. No diffraction peak corresponding to MgO is detected, indicating that either MgO is amorphous, or the amount of crystalline MgO is too small to be detected. However, compared with γ-Al_2O_3, the Al_2O_3(440) peak shows a small left shift for 1MgAl and 5MgAl (Figure 3(a)). Noting that the ionic radius of Mg^{2+} (86 pm) is larger than for Al^{3+} (67.5 pm), the left shift can be ascribed to lattice expansion induced by incorporation of Mg^{2+} into Al_2O_3, whereby non-stoichiometric or stoichiometric $MgAl_2O_4$ forms. On 15Ni/1MgAl-ap and 15Ni/5MgAl-ap, NiO diffraction peaks are detected (Figure 3(b)). In the presence of MgO, a slight shift of the main NiO(200) towards the MgO(200) diffraction at 42.9° can point to a NiMgO solid solution[41]. To further check the change in structure brought by the possible formation of a $MgAl_2O_4$ layer on top of Al_2O_3, Ni supported on spinel $MgAl_2O_4$ was synthesized as a reference. From its XRD pattern, the left shift of the

NiO(200) peak is observed here as well, suggesting that some Mg from $MgAl_2O_4$ migrates into NiO producing a NiMgO solid solution.

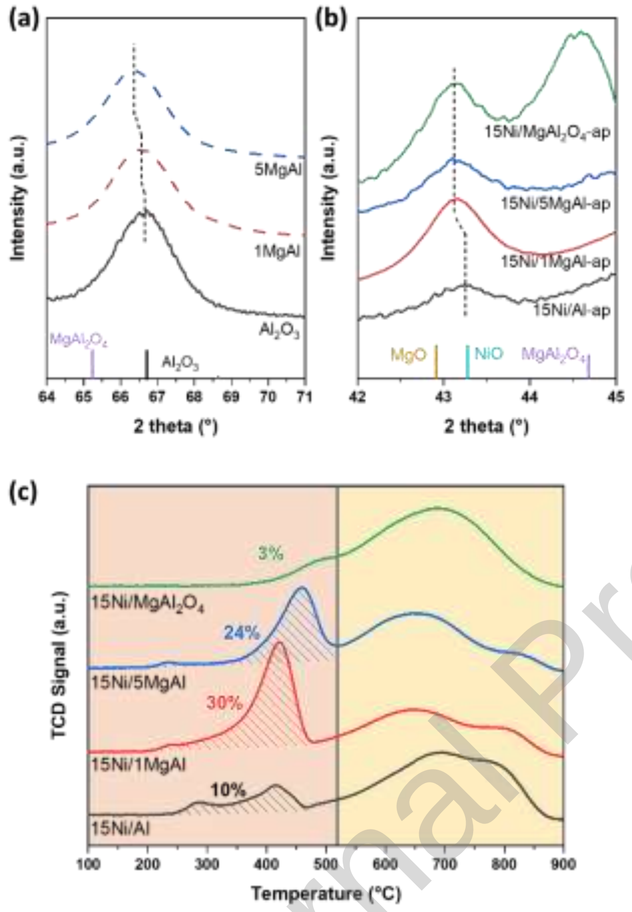

Figure 3. (a) XRD patterns of Al_2O_3, 1MgAl, 5MgAl, zoomed to the Al_2O_3(440) diffraction, and (b) as-prepared 15Ni/Al, 15Ni/1MgAl, 15Ni/5MgAl, 15Ni/$MgAl_2O_4$, zoomed to the NiO(200) main diffraction. (c) H_2-TPR profiles of 15Ni/Al, 15Ni/1MgAl, 15Ni/5MgAl and 15Ni/$MgAl_2O_4$. Vertical dashed line in a and b: indicator of diffraction shift. The shaded areas and numbers in c represent the fraction of “free” NiO. Brown overlay: region of “free” NiO reduction, yellow overlay: region of “fixed” NiO reduction.

H_2-TPR is used to determine how MgO as an intermediate layer modifies the interaction between NiO and Al_2O_3. The reduction profiles from 100 °C to 900 °C are displayed in Figure 3(c). According to literature, reduction of two kinds of Ni^{2+} is observed in the TPR profiles[42-44]. The peaks at lower temperature (< 525 °C) correspond to the reduction of NiO loosely interacting with Al_2O_3 – called “free” NiO. Those at higher temperature (> 525 °C) are due to reduction of NiO strongly interacting with Al_2O_3 and/or Ni^{2+} inside Al_2O_3, forming non-stoichiometric or stoichiometric nickel aluminate – termed “fixed” NiO. This is consistent with the XRD result for reduced 15Ni/Al (Figure S4(b)), where the shift of the Al_2O_3(440) diffraction persists, meaning that incorporated Ni^{2+} (“fixed” NiO) remains unreducible at 600 °C and can hence be considered as “fixed” NiO in the TPR profile. Likewise, the XANES region of the Ni K edge spectra recorded from 15Ni/Al during H_2-TPR and their linear combination fitting (LCF) results confirm that the reduction temperature of incorporated Ni^{2+} is 150 °C higher than “free” NiO (Figure S6). NiO-MgO solid solutions also have a high reduction temperature, typically between 600 and 800 °C [23, 41]. However, given the presence of NiO next to the NiO-MgO solid solution, as suggested by XRD, it is likely that H_2 gets activated at lower temperature on reduced “free” NiO and spills over to the solid solution, leading only to a right shift of the reduction peak in the TPR profiles[19].

By integrating the respective peaks in the H_2-TPR profiles, the fraction of “free” NiO has been determined (the shaded area in Figure 3(c) and the fraction is labeled). “Free” NiO comprises only 10 % of all Ni species in 15Ni/Al, indicating most Ni is engaged in strong interaction with Al_2O_3, which leads to new phase formation and restrains the reduction of NiO. When 1 wt% of MgO is used at the NiO-support interface (15Ni/1MgAl), the fraction of “free” NiO increases significantly (Figure 3(c)), which is also reflected in the twofold increase of the amount of exposed Ni after reduction (Table 1). When further increasing the MgO loading to 5wt%, the “free” NiO again decreases somewhat. Given the similar Ni particle size of 15Ni/Al and 15Ni/5MgAl, a proper amount of MgO is thus capable of maintaining more “free” Ni, with concomitant higher availability of metallic Ni after reduction. The XANES region of the Ni K edge spectra for 15Ni/Al-ap, 1Mg15Ni/Al-ap, 15Ni/1MgAl-ap (Figure S6(c)) and the LCF results (Table S2) further confirm that the formation of $NiAl_2O_4$ is suppressed when MgO serves as an intermediate layer between Ni and Al_2O_3. In contrast, when NiO is deposited directly onto $MgAl_2O_4$, having the highest concentration of Mg at the surface (Table S3), there is hardly any “free” NiO present. Considering NiMgO mixed oxide also forms in 15Ni/1MgAl and 15Ni/5MgAl (based on the left shift of the NiO diffraction peak in XRD, Figure 3(b)), while still these two samples show lots of “free” NiO at low reduction temperature, NiO seems to interact very strongly with the $MgAl_2O_4$ support.

Combined with the result of XRD, it is proposed that the effect of adding MgO on γ-Al_2O_3 is twofold. On the one hand, Mg^{2+} cations enter γ-Al_2O_3 forming some non-stoichiometric or stoichiometric $MgAl_2O_4$ spinel (Figure 3(a)). As the spinel positions are now at least in part occupied by Mg^{2+}, Ni^{2+} migration into the support is lessened. Hence, there is more readily reducible “free” Ni and after reduction, more exposed metallic Ni contributes to enhance the reaction rate (Figure 2). On the other hand, NiO interacts with MgO deposited on the γ-Al_2O_3 support. The reducibility of Ni^{2+}, as displayed in Figure 3(c), is promoted by a small amount of Mg^{2+}, but gets inhibited by an excess[41]. Thus, a trade-off exists between the loadings of Ni-Mg-Al, where 1% Mg was found to yield the best reducibility of NiO.

3.3 Adding MgO onto NiO – MgNi/Al

The structure of xMg15Ni/Al catalysts, where an extra MgO/Ni interface is introduced, was first characterized by XRD. In Figure 4(a), the pattern for 15Ni/Al shows a similar left shift of the Al_2O_3(440) peak as discussed in section 3.2. Subsequent deposition of 1% MgO induces no change in peak position, but adding 5% MgO does entail an extra shift in the same direction. This phenomenon is different from MgO directly deposited onto Al_2O_3, where the Al_2O_3(440) peak did show a small shift for 1% MgO (Figure 3(a)). For NiO(200), an apparent left shift is detected in xMg15Ni/Al when the loading of MgO is increased to 5% (Figure 4(b)). Hence, in this sample, MgO reacts with NiO and Al_2O_3, generating both NiMgO mixed oxide and (non-)stoichiometric $MgAl_2O_4$.

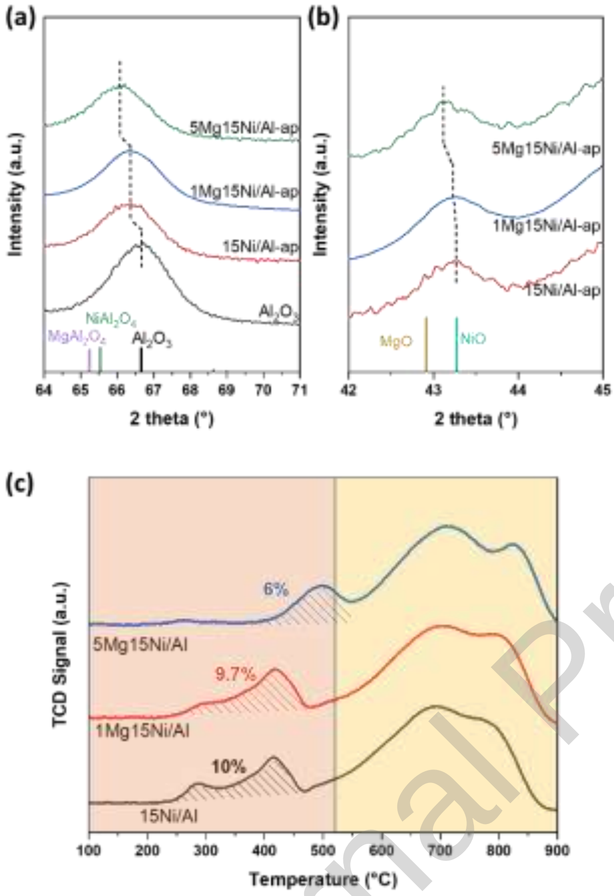

Figure 4. XRD patterns of as-prepared Al_2O_3, 15Ni/Al, 1Mg15Ni/Al and 5Mg15Ni/Al: (a) zoomed to the Al_2O_3(440) peak and (b) zoom onto the NiO(200) diffraction. (c) H_2-TPR profile of 15Ni/Al, 1Mg15Ni/Al and 5Mg15Ni/Al. Vertical dashed line in a and b: indicator of diffraction shift. The shaded areas and numbers present the fraction of "free" NiO. Brown overlay: region of "free" NiO reduction, yellow overlay: region of "fixed" NiO reduction.

H_2-TPR was applied to test the reduction behavior of the xMg15Ni/Al catalyst (Figure 4(c)). With the addition of MgO, the "free" NiO fraction reduces, accompanied by a shift of its reduction peak to higher temperature. Based on the XRD result, the formation of a NiMgO solid solution can be held responsible for these changes in reduction behavior, because the strong interaction between Ni-Mg-O makes reduction of NiO more difficult[41].

3.4 Properties of the MgO-related interfaces

The position of MgO in both configurations is further assessed by SEM-EDX and XPS (Table S1, S2 and Figure S7). The bulk composition from EDX is similar to the theoretical loading. Whereas EDX probes concentrations within a µm layer below the surface, XPS is sensitive to the top few nm. The surface concentration of each element is shown in Table S3. The Mg:Ni ratios of 15Ni/5MgAl and 5Mg15Ni/Al are 1.6 and 2.3, respectively. This result confirms reverse structures on these two samples. In 15Ni/5MgAl, NiO is dispersed on top of MgO, reducing the Mg contribution in XPS, while in 5Mg15Ni/Al, MgO resides both on the surface of Al_2O_3 and on NiO.

DRIFTS was applied to probe the reaction intermediates for conversion of CO_2 towards CH_4 and the possible conversion sites on 15Ni/Al, 1Mg15Ni/Al and 15Ni/1MgAl. First, these samples were treated with CO_2, followed by purging with He (solid lines in Figure S8(a)). Carbonates, including both bidentate (bi-CO_3^{2-}) and monodentate (mono-CO_3^{2-}) with several broad peaks between 1700 -1300 cm^{-1}[45, 46], are present as main adsorbates, showing the samples display similar CO_2 adsorption behavior. After CO_2 treatment and He purging, H_2-TPSR was applied. DRIFT spectra recorded after H_2-TPSR (dashed lines in Figure S8(a)) show the persistence of most adsorbates, with only a minor reduction in carbonates observed on all samples. No features were detected in the CO* region (2000-2150 cm^{-1}) and the C-H stretch region (2800-3050 cm^{-1}) (not shown). The gas products during the H_2-TPSR treatment were monitored by MS, which detected minor CO_2 desorption, followed by a more pronounced CH_4 production (Figure S8(b-d)), indicating that some carbonates desorb forming CO_2 while some actively participating in CH_4 formation. Note that the signal of H_2O, representing the OH removal and the H_2O formation during CO_2 methanation, appears after CH_4 and CO_2, indicating a higher activation barrier of -OH removal. This result is in consistence with previous works[47, 48]. In addition, MgO-containing samples display a small signal at 1740 cm^{-1}, which can be attributed to adsorbed formyl groups (*HCO)[49], indicating some carbonate got converted into *HCO under H_2 treatment.

However, the observed change in surface species detected after H_2-TPSR is small relative to the full carbonates' signal intensity, indicating that only a fraction actively participates in the formation of CH_4. The small extent of changes also suggests that this limited fraction most likely originates solely from carbonate adsorbed near Ni, i.e. at the interfaces Ni/Al_2O_3 and/or MgO/Ni. Since H_2 is only activated on metallic Ni, it can spill over towards the nearby Ni/Al_2O_3 and/or Ni/MgO interface sites, where it can react with adsorbed CO_3^{2-} and form CH_4. In contrast, carbonates adsorbed on oxide surface sites away from Ni, be it MgO or Al_2O_3, are merely spectator. Since the newly formed adsorbed HCO species appear in the DRIFT spectrum of MgO-containing samples after H_2-TPSR, these carbonate species are only partially hydrogenated and hence do not contribute to the CH_4 formation. Possibly, these species migrate away from the Ni/Al_2O_3 and/or Ni/MgO interface, keeping them from being further hydrogenated.

CO_2-TPD tests were carried out on pre-reduced samples to evaluate the CO_2 adsorption ability of the samples (Figure 5(a)). Roughly, two desorption peaks are detected, at low temperature (LT, <200 °C) and high temperature (HT, 200 < T < 350 °C), corresponding to different sites onto which CO_2 is weakly and more strongly adsorbed. Control experiments were applied on Al_2O_3 and 5MgAl (Figure S9), showing a more intense HT desorption peak for 5MgAl than for γ-Al_2O_3, which indicates MgO itself mainly contributes to the strong CO_2 adsorption sites.

Table 2. Quantification result of CO_2-TPD. Black numbers: integrated peak area; Red numbers: results normalized to the amount of metallic Ni exposed.

	LT peak area (a.u.)	HT peak area (a.u.)	Total area (a.u.)

15Ni/Al	1.1	1.1	2.1	2.1	3.2	3.2
1Mg15Ni/Al	0.9	1.0	3.1	3.4	4	4.4
5Mg15Ni/Al	1.2	1.7	4.7	6.7	5.9	8.4
15Ni/1MgAl	2.5	1.3	2.5	1.3	5	2.6
15Ni/5MgAl	2.5	1.5	3.5	2.1	6	3.6

To allow for comparison with TOF, the amount of CO_2 adsorption sites is normalized by the amount of exposed Ni. When MgO is deposited on top of Ni (xMg15Ni/Al), the area of the HT peak increases (Table 2). With increasing MgO loading, the increased HT peak can be attributed to more CO_2 adsorbed on MgO and/or at the MgO/Ni interface. For the 15Ni/xMgAl samples, however, the LT peak begins to increase firstly, while the HT peak only follows upon further addition of MgO (Figure 5(a)). Compared with 15Ni/Al, 15Ni/xMgAl has 2 times more metallic Ni sites (Table 1) and additional MgO sites. Considering MgO contributes to the HT peak (Figure S9), it can be inferred that the LT peak rise rather corresponds to Ni-related adsorption of CO_2. Further, since the LT increase for 15Ni/xMgAl is different from the 15Ni/Al profile (Figure S9), it must be connected to Ni/MgO or Ni/$Mg_xAl_2O_{3+x}$ interface sites, rather than to pure Ni or Ni/Al adsorption. Thus, the CO_2-TPD results reflect the affinity of different surfaces/interfaces to CO_2.

Interestingly, a positive correlation is observed between the TOF for CO_2 methanation (Figure 2(c-d)) and the normalized amount of strong CO_2 adsorption sites (5Mg15Ni/Al > 1Mg15Ni/Al > 15Ni/Al ≈ 15Ni/5MgAl > 15Ni/1MgAl, Table 2), implying the significance of these adsorption sites for the CO_2 activation and conversion.

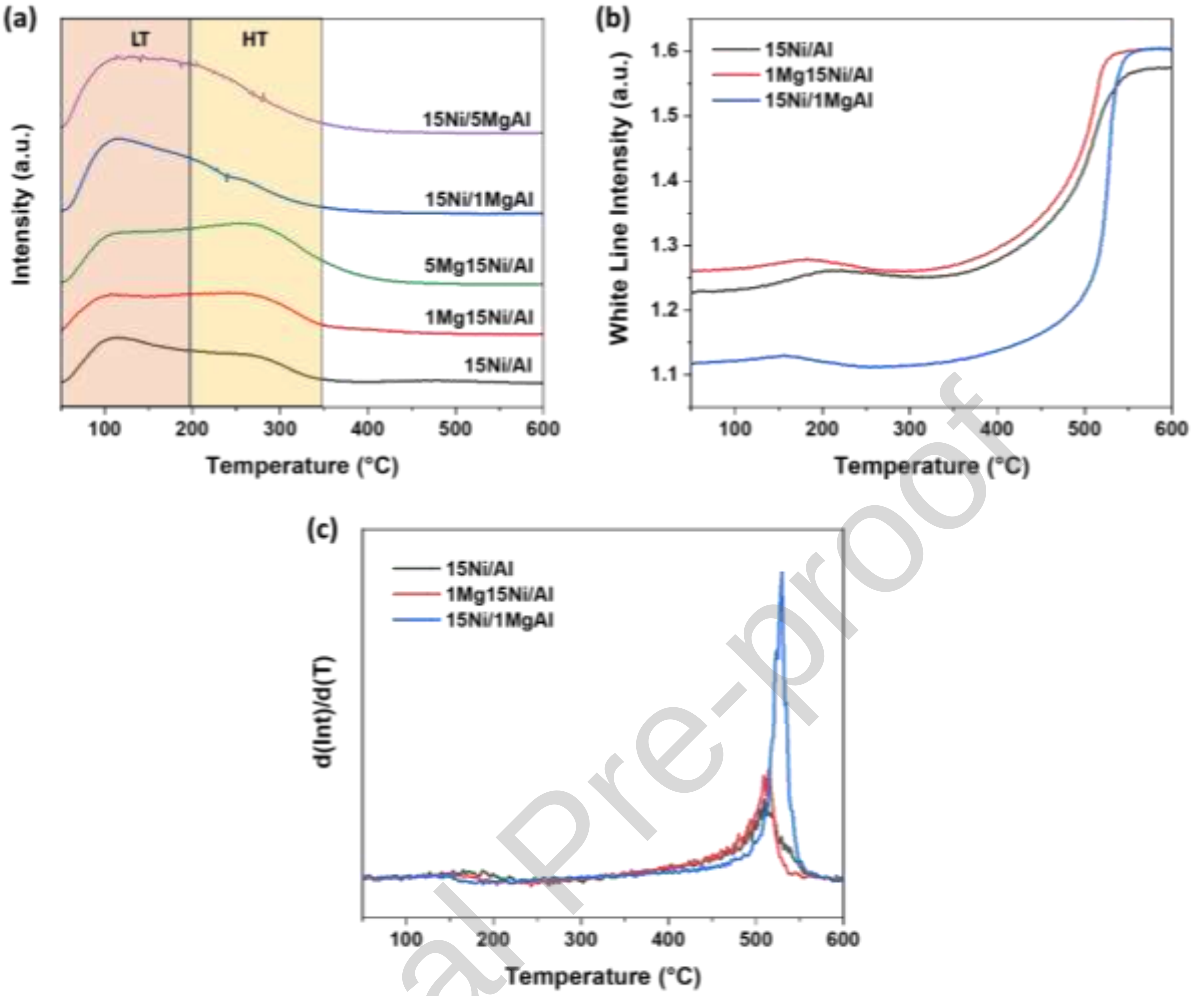

Figure 5. (a) CO_2-TPD profiles of 15Ni/Al, 1Mg15Ni/Al, 5Mg15Ni/Al, 15Ni/1MgAl and 15Ni/5MgAl. All the samples are pre-reduced under 5% H_2/Ar for 30 min at 600 °C. Brown overlay: region of weak adsorption, yellow overlay: region of stronger adsorption. (b) The XANES white line intensity as a function of temperature during CO_2-TPO for reduced 15Ni/Al, 1Mg15Ni/Al and 15Ni/1MgAl. All the samples were reduced with a H_2-TPR session. (c) The first derivative of the Ni K edge XAS white line intensity as a function of temperature during CO_2-TPO for reduced 15Ni/Al, 1Mg15Ni/Al and 15Ni/1MgAl.

The reactivity of the reduced samples with CO_2 was examined further by in situ QXAS during a CO_2-TPO process. The Ni K edge XANES spectra are displayed in Figure S10 (a-c). From these spectra, the white line intensities are extracted and plotted against temperature (Figure 5(b)). The white line intensities at the start of TPO (RT) order as 1Mg15Ni/Al > 15Ni/Al >

15Ni/1MgAl, which is consistent with 15Ni/1MgAl being more reduced than 1Mg15Ni/Al after 600 °C reduction (Table 1). For all samples, a first weak increase appears at the beginning of the temperature ramp, extending up to 150 °C and 200 °C. Considering that the white line drops again thereafter, which cannot happen if Ni gets oxidized, this disturbance is considered to be a consequence of CO_2 adsorption. Starting from 300 °C onwards, the curves rise again, with a steep ascent due to oxidation by CO_2 towards 500 °C. In the final stage of CO_2 oxidation, Mg-containing samples are more extensively oxidized by CO_2 than Ni/Al.

Oxidation of Ni by CO_2 has been observed in several works on Ni(110) and Ni(111) model catalysts by Ambient-Pressure X-ray Photoelectron Spectroscopy. CO_2 is proposed to dissociatively adsorb on the surface of Ni above ambient temperature, where NiO and CO_3^{2-} were detected as evidence. However, the oxidation is limited to the surface due to either a low CO_2 concentration or a low O diffusion rate from the Ni surface into the bulk[50-53]. In previous research on Ni/SiO_2 and pure Ni, Ni oxidation did not take place at temperatures of 600 °C and at 800 °C, respectively[19, 54]. However, when there was formation of active interfaces like Ni/MgO or $Ni/MgAl_2O_4$, bulk phase Ni oxidation did occur. This phenomenon was attributed to metal-support interactions, activating CO_2 at the interface and enabling oxygen transfer into the reduced lattice[19, 54]. In the present work, Ni oxidation is facilitated by the active Ni/Al_2O_3 interface, and the introduction of an additional MgO/Ni or Ni/MgO interface leads to stronger oxidation. Interface sites have been demonstrated to significantly reduce the energy barrier for CO_2 dissociation, while also promoting strong adsorption of CO, thereby facilitating the reaction $CO_2 \rightarrow CO + O_s$[32, 54, 55]. This process results in an increased concentration of surface-bound oxygen species (O), which are known to be mobile on a Ni surface. At elevated temperatures, these O species have the capability to migrate into the metallic bulk, contributing to the formation of subsurface oxygen[53, 56, 57]. The presence of higher concentrations of both surface O and subsurface oxygen leads to a right shift in the equilibrium between Ni + O ↔ NiO, culminating in the transformation of Ni into NiO phases.

The first derivative of the XANES white line intensities was calculated to assess the oxidation rate of these samples. Bulk Ni oxidation for 15Ni/1MgAl occurs fastest at 530 °C, while for the other two samples the highest oxidation rate appears at 500 °C. Comparing the onset of oxidation rate increase, 15Ni/Al and 1Mg15Ni/Al start oxidizing before 15Ni/1MgAl. Their higher rate at low temperature indicates they have a lower energy barrier for oxidation, making them more CO_2-reactive than 15Ni/1MgAl (Figure 5(c)).

To assess whether structural changes such as phase transitions occur during reaction, the local environment of Ni was compared through *in situ* XAS for different states: at the start and end of a 60 min steady-state methanation reaction, and at the start and end of 120 min H_2-CO_2 modulated redox exposure. Representative *in situ* Ni K-edge EXAFS data are presented in the SI (Figure S11). No significant differences in the k-space data are observed between the start and the end of the *in situ* treatment, suggesting that the local structure of the catalyst remains stable during this experiment. The MS monitored the CH_4 formation during the *in situ* XAS experiment and no obvious deactivation was observed for any of the tested catalysts (Figure S12).

To further investigate the dynamic changes of the active sites during reaction, modulation excitation coupled with *in situ* XAS was employed to enhance the surface sensitivity of the bulk technique[37, 58]. MEXAS results at the Ni K edge for reduced 15Ni/Al, 1Mg15Ni/Al and 15Ni/1MgAl during H_2-CO_2 modulation at 300 °C are presented in Figure 6. For all samples, the time-resolved XANES spectra reveal no notable changes with the imposed H_2-CO_2 modulation (blue lines), while the phase-resolved demodulated spectra do display features above noise level. Notable peaks are present in the region of the pre-edge shoulder and of the white line, with strongest intensity for 1Mg15Ni/Al (Figure 6(c)). For comparison, phase-resolved spectra, recorded during a steady-state methanation reaction at 300 °C, show nothing but noise after demodulation (Figure S13. it is assumed that there are periods, while no switching gases during steady-state process).

In the demodulated results (Figure 6(a-c)), anticorrelated peaks are distinguished: the feature at 8335−8340 eV has corresponding peaks at 8347−8360 eV (shown as the blue zones). Anticorrelated means the in-phase angles, where the peak amplitude becomes maximum, of the two features exhibit a difference of 180°. The anticorrelated peaks located at the pre-edge and white line point to redox behavior of Ni[37]. The other signals after demodulation reflect the behavior of reaction intermediates during the periodic excitation[59]. For instance, the MgO-modified samples 15Ni/1MgAl and 1Mg15Ni/Al display an additional sharp feature protruding at the edge position 8333eV (shown as an orange zone), which is far less intense or even absent in Ni/Al. The latter could be an indicator of adsorbed species, being more abundant at a Ni/MgO interface.

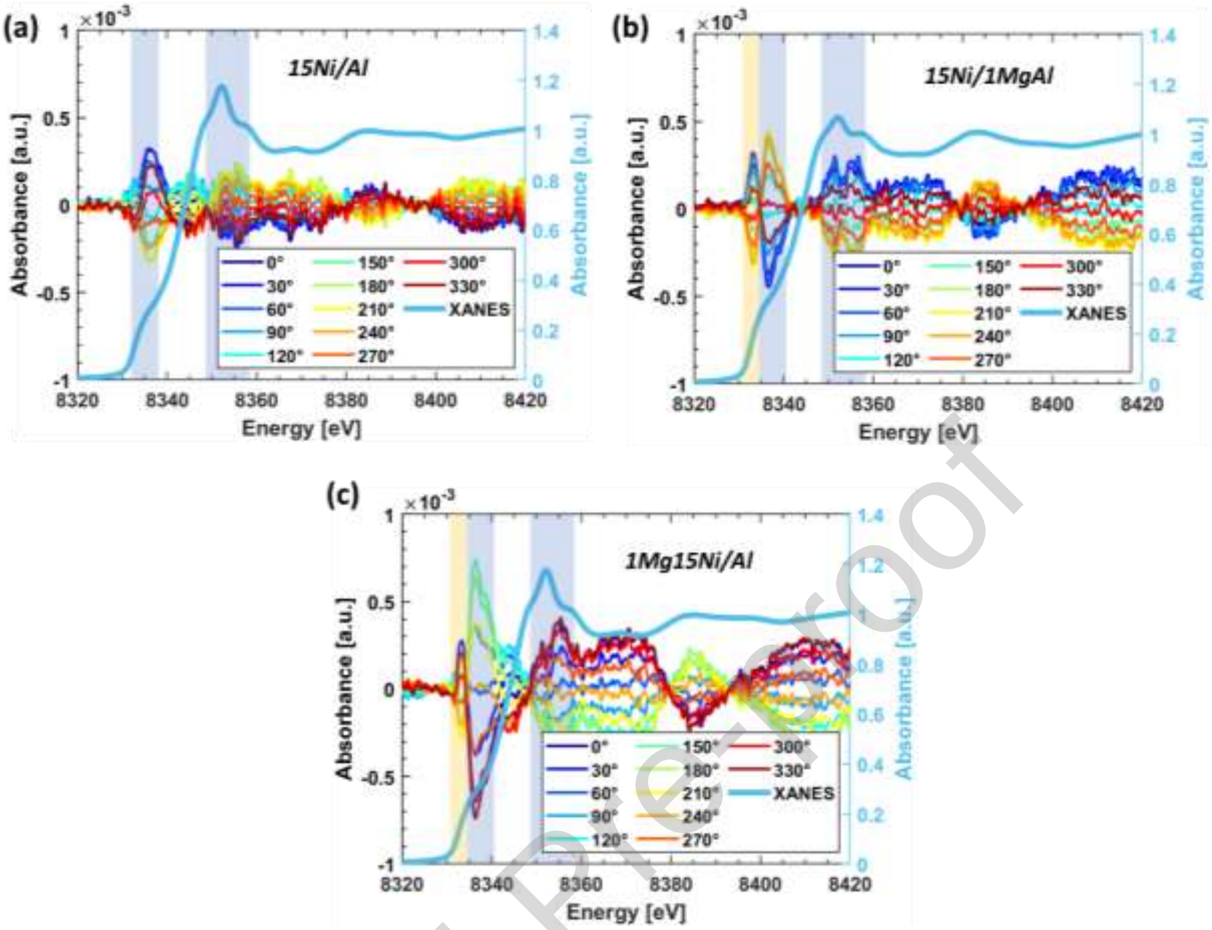

Figure 6. MEXAS results at the Ni K edge for (a) 15Ni/Al, (b) 15Ni/1MgAl and (c) 1Mg15Ni/Al recorded at the Ni K edge during H_2-CO_2 modulation at 300 °C. Last 8 periods are used for the PSD calculation. Blue zones: regions with anticorrelated features; Light blue lines: XANES spectra during modulation; Colored lines: phase-resolved spectra after PSD analysis. Orange zone: protruding feature at the edge position for MgO-containing samples.

Based on prior work, the maximum amplitude of the demodulated spectra yields an estimate of how many active Ni atoms follow the modulation[37, 60]. The amount of responsive Ni atoms on 1Mg15Ni/Al is found to be 2 times higher than on 15Ni/Al, 0.7x10^{3} vs. 0.3x10^{3}, while the number of atoms reacting to the modulation over 15Ni/1MgAl and 15Ni/Al is similar. Consistent with the activity result (Figure 2(d)), the most active sample among these three, 1Mg15Ni/Al, exhibits the highest signal intensity, suggesting it is the most reactive, although it has the lowest number of exposed Ni sites (Table 1). The latter indicates that not so much the surface Ni sites are important for the activity, but rather the interface sites. In particular, the new interface created by MgO modification on top of Ni is intrinsically beneficial for the methanation performance.

Compiling all the characterization data for MgNi/Al leads to a CO_2 methanation scheme, in which the MgO/Ni interface takes up a particular role (Scheme 1). The observed anticorrelation in MEXAS at the Ni K edge indicates that a Mars–van Krevelen mechanism is involved in H_2-CO_2 modulation, representative of the Reverse Water-Gas Shift reaction (RWGS). Herein, CO_2 adsorbs either as carbonate (panel A) or dissociates into CO and O, preferably at the MgO/Ni interface sites because of its lower energy barrier, allowing O species to be incorporated into the Ni lattice (panel B). H_2 on the other hand gets activated on metallic Ni (panel C). From there, it spills over to NiO to react with lattice oxygen (panel D) and to the interface sites, where it hydrogenates adsorbed CO_3^{2-} species to methane (panel E). Carbonates that are located away from interface sites do not get hydrogenated and hence remain visible in DRIFTS. The first hydrogenation of CO at the interface sites leads to formation of formyl groups. The latter can also yield methane, though part of them seems to migrate away from these sites, making them inaccessible for further hydrogenation and preserving them in DRIFTS (panel F).

Whereas the H_2 reduction-CO_2 oxidation of NiO-Ni represents a Mars-Van Krevelen mechanism, involving the exchange of lattice oxygen, the subsequent hydrogenation of adsorbed CO and/or CO_3^{2-} through interaction with adsorbed H rather follows a Langmuir-Hinshelwood mechanism. The latter requires the proximity of Ni for the H supply through spillover and will preferably proceed with species adsorbed near the interface sites, where the energy barrier for activation is lowered. This interpretation highlights a complex interaction between CO_2 activation and the dynamic state of Ni in presence of hydrogen.

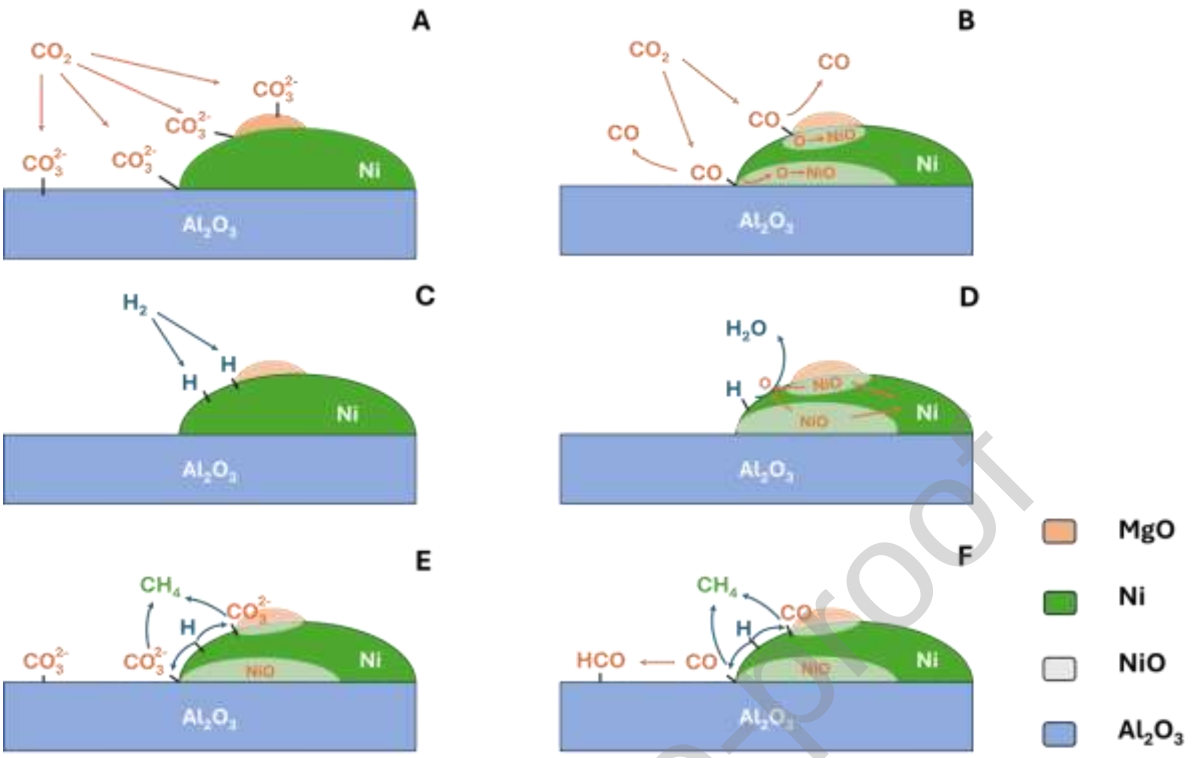

Scheme 1. Schematic diagram of the role of the MgO/Ni interface in CO_2 methanation. Panel A: CO_2 adsorption leading to carbonate formation; panel B: dissociative CO_2 adsorption leading to Ni oxidation; panel C: dissociative H_2 adsorption on metallic Ni; panel D: H_2 oxidation and concomitant NiO reduction; panel E: hydrogenation of adsorbed CO_3^{2-} and H spilling over (combining A and C); panel F: hydrogenation of adsorbed CO and H spilling over (combining B and C). Black connector line: adsorbed surface species.

4. CONCLUSION

This work illustrates the importance of interfaces in a catalytic process. By switching the deposition sequence, catalysts with reverse interface structure, Ni/MgO and MgO/Ni were constructed on Al_2O_3. The CO_2 methanation performance was promoted over both samples compared with unmodified Ni/Al_2O_3, however, with distinct mechanisms.

Over Ni/MgO-Al_2O_3 catalysts, a layer of non-stoichiometric $Mg_xAl_2O_{3+x}$ forms between Ni and Al_2O_3 as confirmed by H_2-TPR, XRD, XPS, EDX and XAS. With a proper amount of MgO, the newly formed layer mitigates interaction between NiO and Al_2O_3, preventing Ni^{2+} from dissolving into the bulk of Al_2O_3. This strategy ensures more metallic Ni active sites becoming reducible at relatively moderate temperature. However, MgO can interact with Ni forming more stable NiMgO as mixed oxide. Thus, a further increase of the deposited MgO amount or the use of stoichiometric $MgAl_2O_4$ exhibits a negative effect on the methanation performance. Over MgO-Ni/Al_2O_3 catalysts, a new MgO/Ni interface was fabricated on top of Ni, which provides strong CO_2 adsorption sites. Ni oxidation started slightly earlier on MgO-Ni/Al_2O_3 as observed via *in situ* QXAS, suggesting that the MgO/Ni interface exhibits unique CO_2 reactivity. MEXAS with H_2/CO_2 modulation further confirms that a Ni-NiO redox mechanism is involved in the CO_2 activation process over a MgO-modified, supported Ni catalyst. The interfaces provide preferential sites for adsorption and activation of CO_2, yielding CO and CO_3^{2-}, which lead to methane after interaction with spilled-over hydrogen. This work demonstrates the concept that careful engineering of interfaces, oxide-metal and/or metal-support, allows to steer the catalyst activity for methanation, which holds promise for practical applications. However, further investigations are needed to assess the reactivity and structural stability of these catalysts in order to meet industrial requirements.

ACKNOWLEDGMENTS

This work is part of a project funded by the Fund for Scientific Research Flanders (project number G032920N). The authors acknowledge the assistance from the ROCK staff for a smooth beamtime (SOLEIL, proposal 20230405). This work was supported by a public grant overseen by the French National Research Agency (ANR) as part of the “Investissements d’Avenir” program (reference: ANR-10-EQPX-45). The authors acknowledge Ir. Thomas Van De Moere for his contribution in experimental works.

REFERENCES

[1] S. Kattel, P. Liu, J.G. Chen, Tuning Selectivity of CO_2 Hydrogenation Reactions at the Metal/Oxide Interface, J. Am. Chem. Soc. 139 (2017) 9739-9754. https://doi.org/10.1021/jacs.7b05362.

[2] Y. Li, Y. Zhang, K. Qian, W. Huang, Metal–Support Interactions in Metal/Oxide Catalysts and Oxide–Metal Interactions in Oxide/Metal Inverse Catalysts, ACS Catal. 12 (2022) 1268-1287. https://doi.org/10.1021/acscatal.1c04854.

[3] T.W. van Deelen, C. Hernández Mejía, K.P. de Jong, Control of metal-support interactions in heterogeneous catalysts to enhance activity and selectivity, Nat. Catal. 2 (2019) 955-970. https://doi.org/10.1038/s41929-019-0364-x.

[4] B. Zhang, Y. Qin, Interface Tailoring of Heterogeneous Catalysts by Atomic Layer Deposition, ACS Catal. 8 (2018) 10064-10081. https://doi.org/10.1021/acscatal.8b02659.

[5] Y. Zhao, V. Girelli, O. Ersen, D.P. Debecker, CO_2 methanation with high-loading mesoporous Ni/SiO_2 catalysts: Toward high specific activity and new mechanistic insights, J. Catal. 426 (2023) 283-293. https://doi.org/10.1016/j.jcat.2023.07.021.

[6] J. Li, E. Croiset, L. Ricardez-Sandoval, Effect of Metal–Support Interface During CH_4 and H_2 Dissociation on Ni/γ-Al_2O_3: A Density Functional Theory Study, J. Phys. Chem. C 117 (2013) 16907-16920. https://doi.org/10.1021/jp402421q.

[7] S. Chen, A.M. Abdel-Mageed, M. Li, S. Cisneros, J. Bansmann, J. Rabeah, A. Brückner, A. Groß, R.J. Behm, Electronic metal-support interactions and their promotional effect on CO_2 methanation on Ru/ZrO_2 catalysts, J. Catal. 400 (2021) 407-420. https://doi.org/10.1016/j.jcat.2021.06.028.

[8] S. Li, Y. Xu, H. Wang, B. Teng, Q. Liu, Q. Li, L. Xu, X. Liu, J. Lu, Tuning the CO_2 Hydrogenation Selectivity of Rhodium Single-Atom Catalysts on Zirconium Dioxide with Alkali Ions, Angew. Chem., Int. Ed. Engl. 62 (2023) e202218167. https://doi.org/10.1002/anie.202218167.

[9] M.-C. Silaghi, A. Comas-Vives, C. Copéret, CO_2 Activation on Ni/γ–Al_2O_3 Catalysts by First-Principles Calculations: From Ideal Surfaces to Supported Nanoparticles, ACS Catal. 6 (2016) 4501-4505. https://doi.org/10.1021/acscatal.6b00822.

[10] W. Liao, C. Tang, H. Zheng, J. Ding, K. Zhang, H. Wang, J. Lu, W. Huang, Z. Zhang, Tuning activity and selectivity of CO_2 hydrogenation via metal-oxide interfaces over ZnO-supported metal catalysts, J. Catal. 407 (2022) 126-140. https://doi.org/10.1016/j.jcat.2022.01.037.

[11] V. Shadravan, V.J. Bukas, G.T.K.K. Gunasooriya, J. Waleson, M. Drewery, J. Karibika, J. Jones, E. Kennedy, A. Adesina, J.K. Nørskov, M. Stockenhuber, Effect of Manganese on the Selective Catalytic Hydrogenation of CO_x in the Presence of Light Hydrocarbons Over Ni/Al_2O_3: An Experimental and Computational Study, ACS Catal. 10 (2019) 1535-1547. https://doi.org/10.1021/acscatal.9b04863.

[12] W.L. Vrijburg, E. Moioli, W. Chen, M. Zhang, B.J.P. Terlingen, B. Zijlstra, I.A.W. Filot, A. Züttel, E.A. Pidko, E.J.M. Hensen, Efficient Base-Metal NiMn/TiO_2 Catalyst for CO_2 Methanation, ACS Catal. 9 (2019) 7823-7839. https://doi.org/10.1021/acscatal.9b01968.

[13] W.L. Vrijburg, G. Garbarino, W. Chen, A. Parastaev, A. Longo, E.A. Pidko, E.J.M. Hensen, Ni-Mn catalysts on silica-modified alumina for CO_2 methanation, J. Catal. 382 (2020) 358-371. https://doi.org/10.1016/j.jcat.2019.12.026.

[14] T.-y. Chen, C. Cao, T.-b. Chen, X. Ding, H. Huang, L. Shen, X. Cao, M. Zhu, J. Xu, J. Gao, Y.-F. Han, Unraveling Highly Tunable Selectivity in CO_2 Hydrogenation over Bimetallic In-Zr Oxide Catalysts, ACS Catal. 9 (2019) 8785-8797. https://doi.org/10.1021/acscatal.9b01869.

[15] S.J. Tauster, Strong metal-support interactions, Accounts of Chemical Research 20 (1987) 389-394. 10.1021/ar00143a001.

[16] Z. Luo, G. Zhao, H. Pan, W. Sun, Strong Metal–Support Interaction in Heterogeneous Catalysts, Adv. Energy Mater. 12 (2022) 2201395. https://doi.org/10.1002/aenm.202201395.

[17] J. Chen, Y. Zhang, Z. Zhang, D. Hou, F. Bai, Y. Han, C. Zhang, Y. Zhang, J. Hu, Metal–support interactions for heterogeneous catalysis: mechanisms, characterization techniques and applications, J. Mater. Chem. A. 11 (2023) 8540-8572. https://doi.org/10.1039/D2TA10036C.

[18] S.A. Theofanidis, V.V. Galvita, H. Poelman, R. Batchu, L.C. Buelens, C. Detavernier, G.B. Marin, Mechanism of carbon deposits removal from supported Ni catalysts, Appl. Catal. B: Environ. 239 (2018) 502-512. https://doi.org/10.1016/j.apcatb.2018.08.042.

[19] Y. Xie, V. De Coster, L. Buelens, H. Poelman, B. Tunca, J.-W. Seo, C. Detavernier, V. Galvita, Tuning CO_2 methanation selectivity via MgO/Ni interfacial sites, J. Catal. 426 (2023) 162-172. https://doi.org/10.1016/j.jcat.2023.07.016.

[20] S.A. Theofanidis, V.V. Galvita, H. Poelman, N.V.R.A. Dharanipragada, A. Longo, M. Meledina, G. Van Tendeloo, C. Detavernier, G.B. Marin, Fe-Containing Magnesium Aluminate Support for Stability and Carbon Control during Methane Reforming, ACS Catal. 8 (2018) 5983-5995. https://doi.org/10.1021/acscatal.8b01039.

[21] P. Lozano-Reis, H. Prats, P. Gamallo, F. Illas, R. Sayós, Multiscale Study of the Mechanism of Catalytic CO_2 Hydrogenation: Role of the Ni(111) Facets, ACS Catal. 10 (2020) 8077-8089. https://doi.org/10.1021/acscatal.0c01599.

[22] H.C. Wu, Y.C. Chang, J.H. Wu, J.H. Lin, I.K. Lin, C.S. Chen, Methanation of CO_2 and reverse water gas shift reactions on Ni/SiO_2 catalysts: the influence of particle size on selectivity and reaction pathway, Catal. Sci. Technol. 5 (2015) 4154-4163. https://doi.org/10.1039/c5cy00667h.

[23] M.-M. Millet, A.V. Tarasov, F. Girgsdies, G. Algara-Siller, R. Schlögl, E. Frei, Highly Dispersed Ni_0/$Ni_xMg_{1-x}O$ Catalysts Derived from Solid Solutions: How Metal and Support Control the CO_2 Hydrogenation, ACS Catal. 9 (2019) 8534-8546. https://doi.org/10.1021/acscatal.9b02332.

[24] F. Koschany, D. Schlereth, O. Hinrichsen, On the kinetics of the methanation of carbon dioxide on coprecipitated NiAl(O), Appl. Catal. B: Environ. 181 (2016) 504-516. https://doi.org/10.1016/j.apcatb.2015.07.026.

[25] T. Van Herwijnen, H. Van Doesburg, W.A. De Jong, Kinetics of the methanation of CO and CO_2 on a nickel catalyst, J. Catal. 28 (1973) 391-402. https://doi.org/10.1016/0021-9517(73)90132-2.

[26] M. Li, H. Amari, A.C. van Veen, Metal-oxide interaction enhanced CO_2 activation in methanation over ceria supported nickel nanocrystallites, Appl. Catal. B: Environ. 239 (2018) 27-35. https://doi.org/10.1016/j.apcatb.2018.07.074.

[27] Y. Guo, S. Mei, K. Yuan, D.-J. Wang, H.-C. Liu, C.-H. Yan, Y.-W. Zhang, Low-Temperature CO_2 Methanation over CeO_2-Supported Ru Single Atoms, Nanoclusters, and Nanoparticles Competitively Tuned by Strong Metal–Support Interactions and H-Spillover Effect, ACS Catal. 8 (2018) 6203-6215. https://doi.org/10.1021/acscatal.7b04469.

[28] K. Feng, J. Tian, M. Guo, Y. Wang, S. Wang, Z. Wu, J. Zhang, L. He, B. Yan, Experimentally unveiling the origin of tunable selectivity for CO_2 hydrogenation over Ni-based catalysts, Appl. Catal. B: Environ. 292 (2021) 120191. https://doi.org/10.1016/j.apcatb.2021.120191.

[29] J. Li, Y. Lin, X. Pan, D. Miao, D. Ding, Y. Cui, J. Dong, X. Bao, Enhanced CO_2 Methanation Activity of Ni/Anatase Catalyst by Tuning Strong Metal–Support Interactions, ACS Catal. 9 (2019) 6342-6348. https://doi.org/10.1021/acscatal.9b00401.

[30] F. Polo-Garzon, T.F. Blum, V. Fung, Z. Bao, H. Chen, Z. Huang, S.M. Mahurin, S. Dai, M. Chi, Z. Wu, Alcohol-Induced Low-Temperature Blockage of Supported-Metal Catalysts for Enhanced Catalysis, ACS Catal. 10 (2020) 8515-8523. https://doi.org/10.1021/acscatal.0c02452.

[31] J.C. Matsubu, S. Zhang, L. DeRita, N.S. Marinkovic, J.G. Chen, G.W. Graham, X. Pan, P. Christopher, Adsorbate-mediated strong metal-support interactions in oxide-supported Rh catalysts, Nat. Chem. 9 (2017) 120-127. https://doi.org/10.1038/nchem.2607.

[32] B. Yan, B. Zhao, S. Kattel, Q. Wu, S. Yao, D. Su, J.G. Chen, Tuning CO_2 hydrogenation selectivity via metal-oxide interfacial sites, J. Catal. 374 (2019) 60-71. https://doi.org/10.1016/j.jcat.2019.04.036.

[33] L. Shen, J. Xu, M. Zhu, Y.-F. Han, Essential Role of the Support for Nickel-Based CO_2 Methanation Catalysts, ACS Catal. 10 (2020) 14581-14591. https://doi.org/10.1021/acscatal.0c03471.

[34] T. Schaaf, J. Grünig, M.R. Schuster, T. Rothenfluh, A. Orth, Methanation of CO_2 - storage of renewable energy in a gas distribution system, Energy, sustain. soc. 4 (2014). https://doi.org/10.1186/s13705-014-0029-1.

[35] C.H. Bartholomew, R.B. Pannell, The stoichiometry of hydrogen and carbon monoxide chemisorption on alumina- and silica-supported nickel, J. Catal. 65 (1980) 390-401. https://doi.org/10.1016/0021-9517(80)90316-4.

[36] C. La Fontaine, S. Belin, L. Barthe, O. Roudenko, V. Briois, ROCK: A Beamline Tailored for Catalysis and Energy-Related Materials from ms Time Resolution to µm Spatial Resolution, Synchrotron Radiat. News 33 (2020) 20-25. https://doi.org/10.1080/08940886.2020.1701372.

[37] V. De Coster, N.V. Srinath, P. Yazdani, H. Poelman, V.V. Galvita, Dual-Element Modulation Excitation XAS to Probe the Redox Surface Chemistry of a Ni–Fe Dry Reforming Catalyst, ACS Catalysis 13 (2023) 12445-12457. 10.1021/acscatal.3c02313.

[38] C.-S. Chen, C.S. Budi, H.-C. Wu, D. Saikia, H.-M. Kao, Size-Tunable Ni Nanoparticles Supported on Surface-Modified, Cage-Type Mesoporous Silica as Highly Active Catalysts for CO_2 Hydrogenation, ACS Catal. 7 (2017) 8367-8381. https://doi.org/10.1021/acscatal.7b02310.

[39] C. Vogt, E. Groeneveld, G. Kamsma, M. Nachtegaal, L. Lu, C.J. Kiely, P.H. Berben, F. Meirer, B.M. Weckhuysen, Unravelling structure sensitivity in CO_2 hydrogenation over nickel, Nat. Catal. 1 (2018) 127-134. https://doi.org/10.1038/s41929-017-0016-y.

[40] D. Beierlein, D. Häussermann, M. Pfeifer, T. Schwarz, K. Stöwe, Y. Traa, E. Klemm, Is the CO_2 methanation on highly loaded Ni-Al_2O_3 catalysts really structure-sensitive?, Appl. Catal. B: Environ. 247 (2019) 200-219. https://doi.org/10.1016/j.apcatb.2018.12.064.

[41] H. Tian, C. Pei, S. Chen, Y. Wu, Z. Zhao, J. Gong, Regulation of Oxygen Activity by Lattice Confinement over $Ni_xMg_{1-x}O$ Catalysts for Renewable Hydrogen Production, Engineering 12 (2022) 62-69. https://doi.org/10.1016/j.eng.2020.08.029.

[42] J.M. Rynkowski, T. Paryjczak, M. Lenik, On the nature of oxidic nickel phases in NiO/γ-Al_2O_3 catalysts, Appl. Catal. A: Gen. 106 (1993) 73-82. https://doi.org/10.1016/0926-860X(93)80156-K.

[43] J. Zieliński, Morphology of nickel/alumina catalysts, J. Catal. 76 (1982) 157-163. https://doi.org/10.1016/0021-9517(82)90245-7.

[44] J.L. Ewbank, L. Kovarik, F.Z. Diallo, C. Sievers, Effect of metal–support interactions in Ni/Al_2O_3 catalysts with low metal loading for methane dry reforming, Appl. Catal. A: Gen. 494 (2015) 57-67. https://doi.org/10.1016/j.apcata.2015.01.029.

[45] P.A.U. Aldana, F. Ocampo, K. Kobl, B. Louis, F. Thibault-Starzyk, M. Daturi, P. Bazin, S. Thomas, A.C. Roger, Catalytic CO2 valorization into CH4 on Ni-based ceria-zirconia. Reaction mechanism by operando IR spectroscopy, Catalysis Today 215 (2013) 201-207. https://doi.org/10.1016/j.cattod.2013.02.019.

[46] D. qin, D. Xie, H. Zheng, Z. Li, J. Tang, Z. Wei, In-Situ FTIR Study of CO2 Adsorption and Methanation Mechanism Over Bimetallic Catalyst at Low Temperature, Catalysis Letters 151 (2021) 2894-2905. https://doi.org/10.1007/s10562-021-03539-2.

[47] J. Huang, X. Li, X. Wang, X. Fang, H. Wang, X. Xu, New insights into CO_2 methanation mechanisms on Ni/MgO catalysts by DFT calculations: Elucidating Ni and MgO roles and support effects, Journal of CO2 Utilization 33 (2019) 55-63. https://10.1016/j.jcou.2019.04.022.

[48] T. Pu, L. Shen, X. Liu, X. Cao, J. Xu, I.E. Wachs, M. Zhu, Formation and influence of surface hydroxyls on product selectivity during CO_2 hydrogenation by Ni/SiO_2 catalysts, J. Catal. 400 (2021) 228-233. https://10.1016/j.jcat.2021.06.008.

[49] I.C.T. Have, J.J.G. Kromwijk, M. Monai, D. Ferri, E.B. Sterk, F. Meirer, B.M. Weckhuysen, Uncovering the reaction mechanism behind CoO as active phase for CO(2) hydrogenation, Nature communications 13 (2022) 324. https://doi.org/10.1038/s41467-022-27981-x.

[50] Y. Zang, J. Cai, Y. Han, H. Wu, W. Zhu, S. Shi, H. Zhang, Y. Ran, F. Yang, M. Ye, B. Yang, Y. Li, Z. Liu, CO_2 Activation on Ni(111) and Ni(110) Surfaces in the Presence of Hydrogen, J. Phys. Chem. Lett. 14 (2023) 4381-4387. https://doi.org/10.1021/acs.jpclett.3c00790.

[51] W. Lin, K.M. Stocker, G.C. Schatz, Mechanisms of Hydrogen-Assisted CO_2 Reduction on Nickel, J. Am. Chem. Soc. 139 (2017) 4663-4666. https://doi.org/10.1021/jacs.7b01538.

[52] C. Heine, B.A. Lechner, H. Bluhm, M. Salmeron, Recycling of CO_2: Probing the Chemical State of the Ni(111) Surface during the Methanation Reaction with Ambient-Pressure X-Ray Photoelectron Spectroscopy, J. Am. Chem. Soc. 138 (2016) 13246-13252. https://doi.org/10.1021/jacs.6b06939.

[53] X. Ding, L. De Rogatis, E. Vesselli, A. Baraldi, G. Comelli, R. Rosei, L. Savio, L. Vattuone, M. Rocca, P. Fornasiero, F. Ancilotto, A. Baldereschi, M. Peressi, Interaction of carbon dioxide with Ni(110): A combined experimental and theoretical study, Phys. Rev. B 76 (2007). https://doi.org/10.1103/PhysRevB.76.195425.

[54] V. De Coster, N.V. Srinath, P. Yazdani, H. Poelman, V.V. Galvita, Does CO_2 Oxidize Ni Catalysts? A Quick X-ray Absorption Spectroscopy Answer, J. Phys. Chem. Lett. 13 (2022) 7947-7952. https://doi.org/10.1021/acs.jpclett.2c01790.

[55] H. Zhang, Z. Liang, C. Huang, L. Xie, H. Wang, J. Hu, Z. Jiang, F. Song, Enhanced dissociation activation of CO2 on the Bi/Cu(111) interface by the synergistic effect, J. Catal. 410 (2022) 1-9. https://doi.org/10.1016/j.jcat.2022.04.001.

[56] S. Mrowec, Z. Grzesik, Oxidation of nickel and transport properties of nickel oxide, J. Phys. Chem. Solids 65 (2004) 1651-1657. https://doi.org/10.1016/j.jpcs.2004.03.011.

[57] J. Cai, Y. Han, S. Chen, E.J. Crumlin, B. Yang, Y. Li, Z. Liu, CO_2 Activation on Ni(111) and Ni(100) Surfaces in the Presence of H_2O: An Ambient-Pressure X-ray Photoelectron Spectroscopy Study, J. Phys. Chem. C 123 (2019) 12176-12182. https://doi.org/10.1021/acs.jpcc.8b11698.

[58] A. Urakawa, T. Bürgi, A. Baiker, Sensitivity enhancement and dynamic behavior analysis by modulation excitation spectroscopy: Principle and application in heterogeneous catalysis, Chem. Eng. Sci. 63 (2008) 4902-4909. https://doi.org/10.1016/j.ces.2007.06.009.

[59] M.-A. Serrer, A. Gaur, J. Jelic, S. Weber, C. Fritsch, A.H. Clark, E. Saraçi, F. Studt, J.-D. Grunwaldt, Structural dynamics in Ni–Fe catalysts during CO_2 methanation – role of iron oxide clusters, Catal. Sci. Technol. 10 (2020) 7542-7554. https://doi.org/10.1039/d0cy01396j.

[60] A. Gaur, T.M. Hartmann Dabros, M. Høj, A. Boubnov, T. Prüssmann, J. Jelic, F. Studt, A.D. Jensen, J.-D. Grunwaldt, Probing the Active Sites of MoS_2 Based Hydrotreating Catalysts Using Modulation Excitation Spectroscopy, ACS Catal. 9 (2019) 2568-2579. https://doi.org/10.1021/acscatal.8b04778.

Graphical abstract

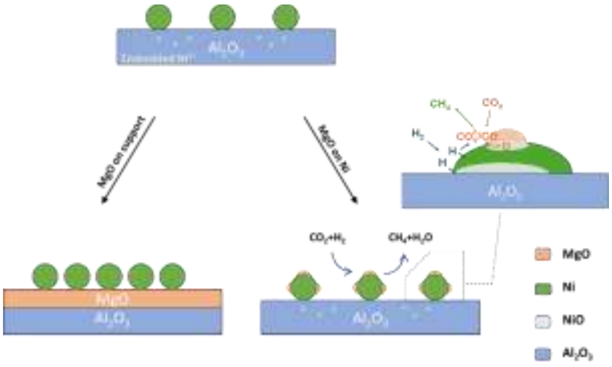

Declaration of Competing Interest

The authors declare that they have no known competing financial interests or personal relationships that could have appeared to influence the work reported in this

Highlights:

- Catalysts with spatially reversed interface structure, Ni/MgO-Al_2O_3 and MgO-Ni/Al_2O_3, exhibit distinct catalytic properties.
- MgO in between Ni and Al_2O_3 mitigates their interaction, i.e. Ni/MgO-Al_2O_3.
- Depositing MgO on Ni generates a new MgO/Ni interface, i.e. MgO-Ni/Al_2O_3.
- CO_2 gets activated at the interface sites, yielding CO and O that oxidizes Ni.
- CO_2 methanation follows from hydrogenation of carbonate and adsorbed CO.